Understanding ordered structure in hematite nanowhiskers synthesized via thermal oxidation of iron-based substrates

Lai, Ming Wei; Kurata, Hiroki

Materials and Design 191 (2020) 108596

Contents lists available at ScienceDirect

Materials and Design

journal homepage: www.elsevier.com/locate/matdes

Understanding ordered structure in hematite nanowhiskers synthesized via thermal oxidation of iron-based substrates

Ming-Wei Lai, Hiroki Kurata *

Institute for Chemical Research, Kyoto University, Uji, Kyoto 6110011, Japan

HIGHLIGHTS

- α-Fe_2O_3 nanowhiskers (NWs) with (001) basal faces synthesized via thermal oxidation of iron-based substrates are strained.
- The ordered structure in the α-Fe_2O_3 (NWs) is periodic interplanar gap expansions induced by oxygen vacancy accumulations.
- The ordered structure forms to accommodate tensile strain.
- Integrating negative-spherical-aberration imaging and monochromated EELS is effective in analyzing strained metal oxides.

GRAPHICAL ABSTRACT

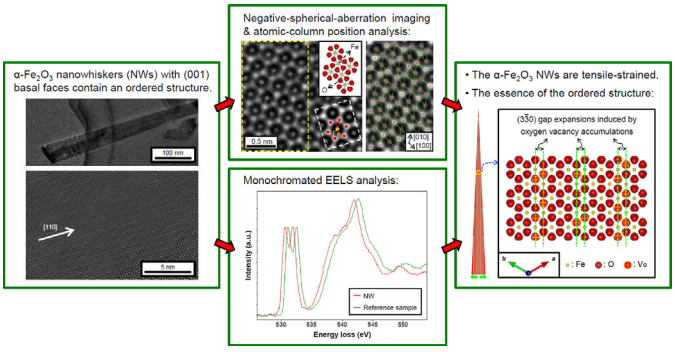

ARTICLE INFO

Article history:
Received 15 October 2019
Received in revised form 19 February 2020
Accepted 21 February 2020
Available online 21 February 2020

Keywords:
α-Fe_2O_3
Nanowhisker
Ordered structure
NCSI
Monochromated EELS

ABSTRACT

Hematite (α-Fe_2O_3) nanowhiskers (NWs) with (001) basal faces synthesized via thermal oxidation of iron-based substrates are known to contain an ordered structure. The ordered structure has been identified to be related to oxygen vacancy ordering. However, the cause of its formation remains a mystery. In this study, with a high-resolution transmission electron microscopy (HR-TEM) investigation based on negative-Cs imaging (NCSI) and atomic-column position analysis, we observed tensile strain in the above-mentioned α-Fe_2O_3 NWs and revealed that the ordered structure was actually periodic interplanar gap expansions induced by oxygen vacancy accumulations. These findings were further confirmed in a monochromated electron energy loss spectroscopy (EELS) analysis of the α-Fe_2O_3 NWs. The EELS data indicated that, in comparison to pristine α-Fe_2O_3, the α-Fe_2O_3 NWs possessed expanded average Fe—O and O—O interatomic distances and were oxygen-deficient. Clarifying oxygen deficiency in the α-Fe_2O_3 NWs was not attributed to an insufficient oxygen supply during the NW growth, we concluded the ordered structure formed to accommodate tensile strain in the α-Fe_2O_3 NWs. This work demonstrates the applicability of integrating NCSI and monochromated EELS for the examination of strain-induced microstructural and microchemical variations in lightly strained metal oxides.

1. Introduction

One-dimensional hematite (α-Fe_2O_3) nanostructures have recently attracted intense research interest because they are promising photoanode materials for photoelectrochemical water splitting. Constructing α-Fe_2O_3 photoanodes with arrayed one-dimensional α-

* Corresponding author.
E-mail address: kurata@eels.kuicr.kyoto-u.ac.jp (H. Kurata).

https://doi.org/10.1016/j.matdes.2020.108596

Fe_2O_3 nanostructures removes the performance limitation imposed by the inherently short hole diffusion length of α-Fe_2O_3 and can improve the electron collection efficiency [1]. Large-area synthesis of arrayed α-Fe_2O_3 nanowhiskers (NWs) can be simply and economically realized through thermal oxidation of an iron-based substrate [2–4]. In the situation the oxidation temperature is below 570 °C, an iron oxide scale composed of a magnetite (Fe_3O_4) layer and an α-Fe_2O_3 layer is expected to initially form on the iron-based substrate. The interfacial stress between these two scale layers then becomes a driving force that pumps iron atoms toward the outmost surface, thereby governing the growth of α-Fe_2O_3 NWs [5].

In microstructural studies of α-Fe_2O_3 NWs synthesized via the thermal oxidation route, researchers have typically observed superstructure modulation in high-resolution transmission electron microscopy (HR-TEM) images of NWs with (001) basal faces. The superstructure modulation indicates the presence of an ordered structure in the NWs, which has long been regarded as ordered oxygen-deficient planes [3,6,7]. A small number of oxygen vacancies in an α-Fe_2O_3 photoanode is indicative of a higher majority carrier density for the photoanode [8,9]. Thus, the reverse flow of electrons from the photoanode inside toward the semiconductor-liquid junction is restrained during photoelectrochemical reactions [10]. On the basis of this interpretation, the ordered structure is thought to improve the photoelectrochemical performance of the host α-Fe_2O_3 NWs. It is a long-standing aspiration for understanding the formation of the ordered structure. Chen et al. claimed the ordered oxygen vacancy planes in α-Fe_2O_3 NWs synthesized via a plasma oxidation process formed to relax stress originating from the lattice mismatch between α-Fe_2O_3 and Fe [11]. However, as they did not anticipate the formation of a multilayered iron oxide scale, their argument does not explain the analogous phenomenon observed in α-Fe_2O_3 NWs synthesized via thermal oxidation of iron-based substrates. According to our own literature survey, no convincing explanation for the formation of the ordered structure has been reported.

For transition metal oxides whose metal cations can adapt to multiple oxidation states, the oxygen vacancy formation energy is reduced by the introduction of tensile strain which to some degree relieves the electron-electron electrostatic repulsion along the broken bonds [12]. In view of the fact that the growth of α-Fe_2O_3 NWs synthesized via the thermal oxidation route is governed by the interfacial stress between the layers of the iron oxide scale, it is reasonable to deduce the emergence of the ordered structure is related to strain. Because the lattice framework of α-Fe_2O_3 is comprised of oxygen anions, analytical methods that can provide information about the spatial arrangement of oxygen atoms are highly demanded for proving this deduction. Following the development of spherical-aberration (Cs) correction for TEM, HR-TEM analysis based on negative-Cs imaging (NCSI) is now available. It is recognized as a powerful technique for imaging low-atomic-number elements, such as oxygen and nitrogen [13–16]. Herein, we report the first NCSI-based HR-TEM observation of α-Fe_2O_3 NWs with (001) basal faces synthesized via the thermal oxidation route. By performing a positional analysis of the detected oxygen columns, we revealed the essence and formation reason of the ordered structure within the α-Fe_2O_3 NWs. The findings of the HR-TEM investigation were further confirmed in a monochromated electron energy loss spectroscopy (EELS) analysis of the α-Fe_2O_3 NWs. This work demonstrates that the integration of NCSI and monochromated EELS is an effective means by which to analyze strain-induced microstructural and microchemical variations in lightly strained metal oxides.

2. Experimental details

The α-Fe_2O_3 NWs investigated in the present study were grown on an ultrasonically cleaned 45 Permalloy sheet (The Nilaco Corp.) by atmospheric thermal oxidation at 550 °C for 20 h. The morphology of the as-synthesized α-Fe_2O_3 NWs (Fig. S1) is similar to that of α-Fe_2O_3 NWs synthesized via thermal oxidation of iron foils in a 200 Torr pure oxygen atmosphere [5]. HR-TEM and EELS were performed with a monochromator-equipped double-Cs-corrector transmission/scanning transmission electron microscope (TEM/STEM) (JEM-ARM200F, JEOL Ltd.) operated at an acceleration voltage of 200 kV. The Cs value for HR-TEM imaging was set to −14 μm. EELS acquisitions of the O K-edge and Fe $L_{2,3}$-edge were performed with the scanning transmission electron microscopy (STEM)-EELS method under the dual-EELS mode [17], for which the spectrometer (GIF Quantum ERS, Gatan Inc.) was focused on the zero-loss peak (ZLP); the convergence and collection semi-angles were 32.3 and 28.2 mrad, respectively, and the energy dispersion was 0.05 eV/channel. Each resultant EELS spectrum was obtained from a summation of 10,000 spectra according to a 100 × 100 EELS spectrum image (Fig. S2). The ZLP full-width-at-half-maximum (FWHM) values for acquiring the O K-edge spectra and Fe $L_{2,3}$-edge spectra were 0.25 and 0.2 eV, respectively (Fig. S3). HR-TEM image simulations were carried out with the xHREM program (HREM Research Inc.). The positional analysis of the detected atomic columns was performed using the PPA DigitalMicrograph plug-in (HREM Research Inc.).

3. Results and discussion

A HR-TEM image of an as-synthesized α-Fe_2O_3 NW with (001) basal faces is shown in Fig. 1a, in which there is clear superstructure modulation. The relation between the geometric shape and the crystallographic orientation of the α-Fe_2O_3 NW is illustrated in Fig. 1b. According to the fast-Fourier-transform (FFT) patterns of the marked areas in Fig. 1a (Fig. 1c and d), the superstructure modulation period is five times the interplanar spacing of the $(3\bar{3}0)$ planes at the NW edge, yet it becomes twice of that at the inner part. Both of these modulation periods have been reported previously with the ordered structure was regarded as ordered oxygen-deficient planes [3,6]. However, this is the first report of their combined presence in a single α-Fe_2O_3 NW. Our finding suggests the period of the ordered structure is determined by the local structural or geometric characteristics of the NW. Because the NW edge and the NW bulk were found predominantly different in thickness, we considered this factor determined the period of the ordered structure.

The HR-TEM image in Fig. 1a was acquired with a relatively large overfocus setting to make the superstructure modulation more visible. However, the excessive overfocus leaded to a drawback that the oxygen columns were unable to be visualized. To ascertain the microstructural essence of the superstructure modulation, we adjusted the overfocus to ~6 nm to satisfy the NCSI criterion (Fig. S4). A bright-atomic-contrast HR-TEM image of the area enclosed within the red dotted box in Fig. 1a is shown in Fig. 2a. A simulated HR-TEM image of an ideal α-Fe_2O_3 lattice with a specimen thickness of 6.9 nm and an overfocus value of 6 nm is superimposed on this experimental image. The yellow arrows mark the positions corresponding to the dark stripes in the superstructure modulation in Fig. 1a. It is now clear that the crystallographic position of each dark stripe is at the interplanar gap between two adjacent $(3\bar{3}0)$ planes, which we designate as a $(3\bar{3}0)$ gap. With a careful examination of Fig. 2a, we noticed that the $(3\bar{3}0)$ gaps corresponding to the dark stripes were also darker than their nearby ones, which was mainly due to lower image intensity of many of the areas each between two neighboring oxygen columns laying to either side of a dark stripe (Fig. S5). This finding implies a number of the oxygen columns flanking the dark stripes are lower in column occupancy or considerably displace from the neutral positions.

Using the peak pairs analysis algorithm [18], we extracted the positions of the atomic-columns enclosed within the yellow dashed box in Fig. 2a and constructed a set of O—O and Fe—O column pairs whose base vectors are parallel to the [100] and [010] directions (Fig. 2b). It can be observed that the lengths of these atomic-column pairs and the angles between joint atomic-column pairs become increasingly

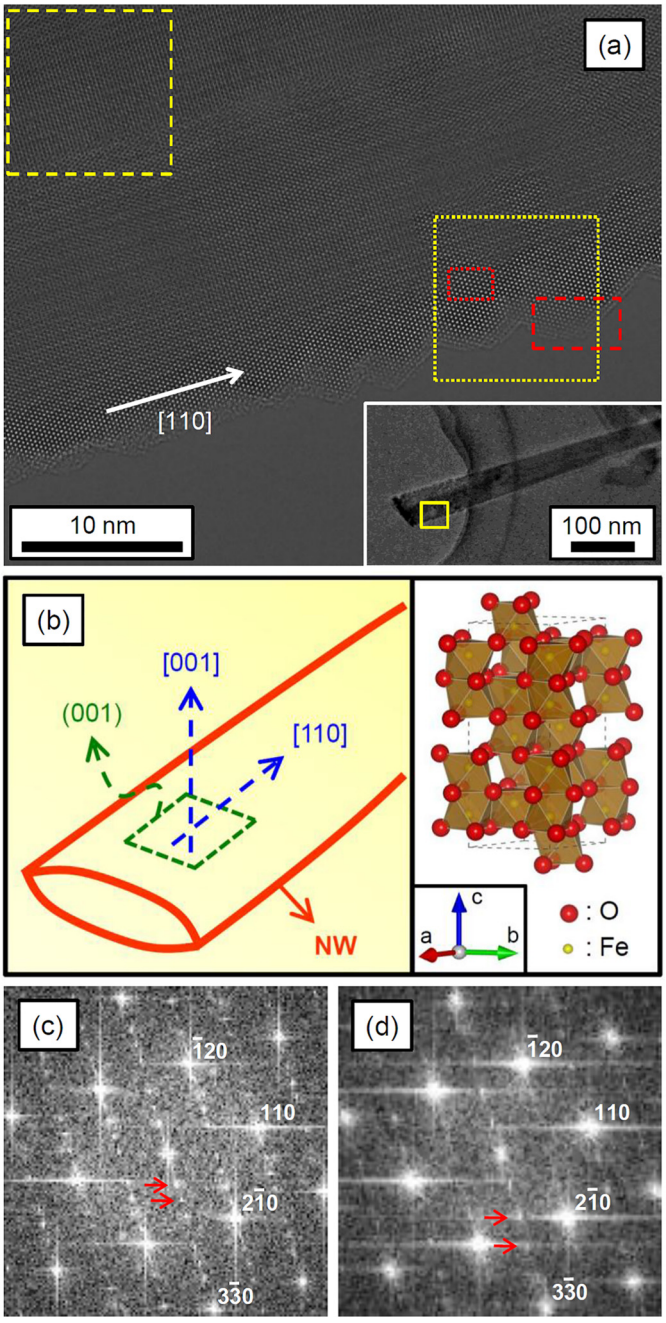

Fig. 1. (a) HR-TEM image of an as-synthesized α-Fe_2O_3 NW with (001) basal faces. The boxed region in the inset TEM image shows the location of HR-TEM observation. (b) Relation between the geometric shape and the crystallographic orientation of the α-Fe_2O_3 NW. At right is shown the crystallographic unit cell of α-Fe_2O_3. (c) and (d) FFT patterns of the areas respectively enclosed within the yellow dashed and yellow dotted boxes in (a). The repetitions of the extra spots are indicated by the red arrows.

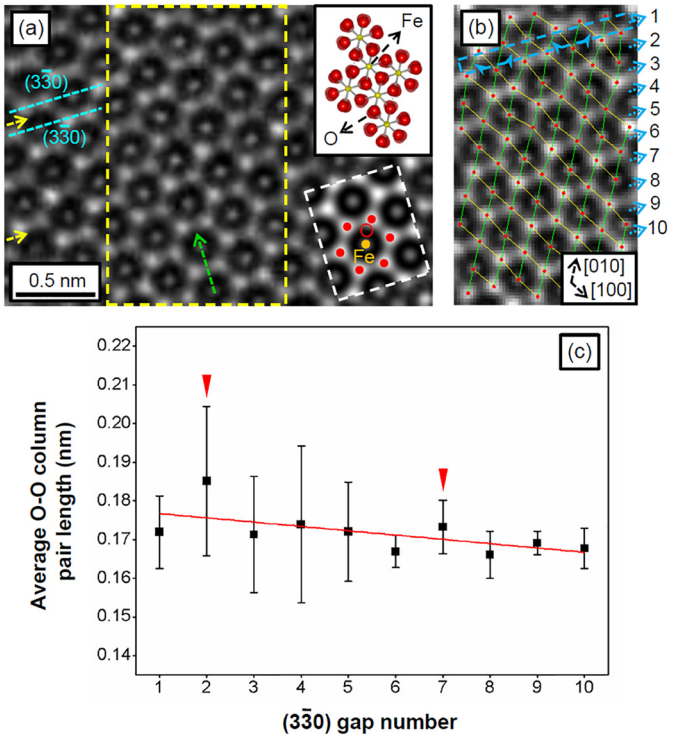

Fig. 2. (a) Bright-atomic-contrast HR-TEM image of the area enclosed within the red dotted box in Fig. 1a. The positions corresponding to the dark stripes are indicated by the yellow arrows. The green arrow indicates the direction of thickness increase. The upper inset shows the structural model of the α-Fe_2O_3 unit cell in the [001] direction. The lower inset is the simulated HR-TEM image. (b) Atomic-column position analysis of the region enclosed within the yellow dashed box in (a). Column pairs with the base vector parallel to the [100] direction are marked by the yellow lines, and column pairs with the base vector parallel to the [010] direction by the green lines. (c) Average O—O column pair lengths for the numbered $(3\bar{3}0)$ gaps in (b). The linear fit of the data is indicated by the red line. The red arrows indicate the $(3\bar{3}0)$ gaps corresponding to the dark stripes. In (b), the dashed box encloses $(3\bar{3}0)$ gap 1, and the blue arrows indicate the O—O column pairs astride this $(3\bar{3}0)$ gap.

irregular as the local thickness of the NW increases. This indicates the presence of thickness-dependent distortion in the α-Fe_2O_3 NW lattice. The atomic-column pair set was further divided into ten segments (the upper and lower edges were excluded) each corresponded to a numbered $(3\bar{3}0)$ gap in Fig. 2b. Estimating the average O—O column pair length for each numbered $(3\bar{3}0)$ gap (Fig. 2c), we observed a trend that the average O—O column pair length for a $(3\bar{3}0)$ gap increased with the local NW thickness became thicker. Therefore, the thickness-dependent lattice distortion should be a reflection of the presence of thickness-dependent tensile strain in the α-Fe_2O_3 NW. Another noteworthy point in Fig. 2c is that the average O—O column pair lengths for $(3\bar{3}0)$ gaps corresponding to the dark stripes (i.e., $(3\bar{3}0)$ gaps 2 and 7) display apparent positive quantity deviations from the fitted data trend. This explains why these two $(3\bar{3}0)$ gaps are relatively darker. More specifically, this indicates that the dark stripes are related to $(3\bar{3}0)$ gap expansions.

Carrying out a close inspection to $(3\bar{3}0)$ gap 2 in Fig. 2b, we found the configuration of the oxygen columns flanking this defect-associated $(3\bar{3}0)$ gap exhibited a non-negligible deviation from the ideal condition; also, the column displacements were found lacking uniformity in terms of quantity and vector (Fig. S6). Such a situation implies the ordered dark stripes cannot be simply attributed to pure lattice modulation like the case in a strained $LaCoO_3$ film [19]. It is known, for tensile-strained transition metal oxides, chemical expansion arising from oxygen vacancy formation provides an alternative way in contrast to sheer lattice distortion to accommodate tensile strain [20], for which a situation that oxygen vacancies distribute orderly has also been reported [21,22]. On the basis of our microstructural observation result, it is possible that the dark stripes result from ordered oxygen vacancy formation. In truth, using low-angle annular dark-field (LAADF)-STEM, Lee et al. have found oxygen vacancy ordering in α-Fe_2O_3 NWs synthesized via thermal oxidation of a $Fe_{64}Ni_{36}$ substrate [6]. It should be noted that an individual oxygen column in the (001) planes of α-Fe_2O_3 actually consists of three sub-columns whose centers are slightly apart from each other; this is illustrated in the upper inset of Fig. 2a. Therefore, once there is an uneven oxygen vacancy accumulation in the sub-columns, the projected potential center of this oxygen column

will shift from its neutral position. This mechanism and the accompanying chemical expansion make a reasonable explanation to the irregular displacements of the oxygen columns flanking the dark stripes, because the conditions of oxygen vacancy accumulation for these oxygen columns can be different from each other. Another point worth to mention is that, in the view of our argument, the dark stripes (i.e., the expanded $(3\bar{3}0)$ gaps) must result in width reductions of their neighboring $(3\bar{3}0)$ gaps. Therefore, in Fig. 2c, the relative reductions of the average O—O column pair lengths for $(3\bar{3}0)$ gaps 1, 3, 6, and 8 also suggest the ordered dark stripes are periodic $(3\bar{3}0)$ gap expansions induced by oxygen vacancy accumulations. We should emphasize that our HR-TEM investigation delivers a new interpretation of the ordered structure different from that suggested in the previous studies, in which the ordered structure is considered to be oxygen-deficient $(3\bar{3}0)$ planes periodically distributing in every five or ten times the interplanar spacing of the $(3\bar{3}0)$ planes [3,6,7]. Since Cs-uncorrected HR-TEM was employed in the previous studies, they were unable to detect the oxygen columns in the α-Fe_2O_3 NWs, which prevented them from obtaining precise structural informational of the ordered structure.

Because no apparent dark stripes were observed at the very edge of the α-Fe_2O_3 NW in Fig. 1a, the situation of atomic-column arrangement in this region can be valuable information compared with the analysis results shown in Fig. 2. The bright-atomic-contrast HR-TEM image of the area within the red dashed box in Fig. 1a is shown in Fig. 3a, where the atomic-column configuration is fairly regular. Atomic-column position analysis was performed on the area enclosed within the yellow dashed box in Fig. 3a, and the related results are shown in Fig. 3b. It can be observed that at this very edge area, there is still a weak positive dependence between the average O—O column pair length for a $(3\bar{3}0)$ gap and the local NW thickness. The standard deviation values for the data points in Fig. 3b are in the range between 5.3 and 9.9 pm. A comparable result was reported by Gauquelin et al. [23]; in their study, the precision of NCSI on the position determination of oxygen columns in bulk-like $NdGaO_3$ was measured to be 12.97 pm and was predominantly limited by image distortions. The small standard deviation values in Fig. 3b indicate the sample drift, environmental interference, and aberration parameters fluctuation were effectively suppressed in our HR-TEM observation. If the minute amount of tensile strain and surface relaxation at the very edge of the α-Fe_2O_3 NW, which to some degree deteriorate the regularity of the atomic-column arrangement, are overlooked, the precision of our NCSI-based atomic-column position analysis is considered to be better than 10 pm. Therefore, in Fig. 2c, the relatively large standard deviation values for the data points corresponding to $(3\bar{3}0)$ gaps 1 to 5 are indeed due to more severe local lattice distortion at the thicker region. To sum up, thickness-dependent tensile strain is present in the α-Fe_2O_3 NW, for which the strain accommodation is realized by lattice distortion and periodic $(3\bar{3}0)$ gap expansions suggested to be induced by oxygen vacancy accumulations.

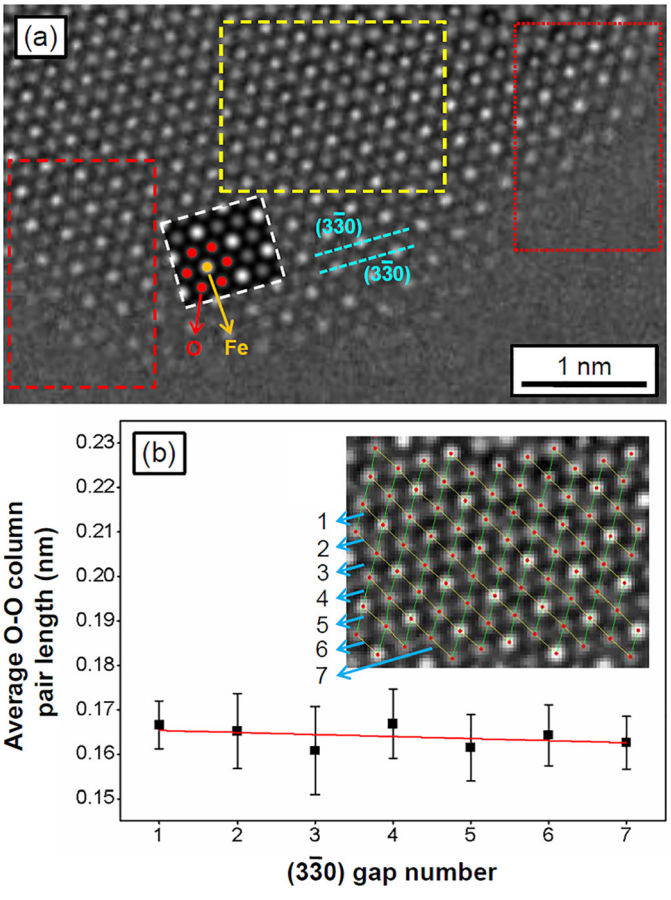

Fig. 3. (a) Bright-atomic-contrast HR-TEM image of the area enclosed in the red dashed box in Fig. 1a. The inset shows a simulated HR-TEM image with a specimen thickness of 1.37 nm and an overfocus value of 6 nm. (b) Average O—O column pair lengths for the numbered $(3\bar{3}0)$ gaps indicated in the inset atomic-column position analysis result that obtained in the region enclosed within the yellow dashed box in (a). The linear fit of the data is indicated by the red line.

A monochromated EELS analysis was performed to examine interatomic distances and evaluate oxygen deficiency in the studied α-Fe_2O_3 NWs. The O K-edge EELS spectra of an as-synthesized α-Fe_2O_3 NW with (001) basal faces and a stoichiometric α-Fe_2O_3 reference sample (commercial α-Fe_2O_3 powder, purchased from Sigma-Aldrich Inc., had been annealed at 500 °C in air for 20 h) are shown in Fig. 4a. The spectra have been normalized to the maximum of peak A1. The sample orientations for the EELS experiment were confirmed to be that the incident electron beam was nearly parallel to the [001] direction of the α-Fe_2O_3 NW and the $[2\bar{2}1]$ direction of the reference sample. Normally, the onset of an O K-edge core-excitation spectrum of α-Fe_2O_3 is considered to be at the first inflection point in the spectrum and is linked with the conduction band minimum (CBM) of α-Fe_2O_3 [24]. Considering the initial rise of the NW O K-edge EELS spectrum might include signal contributions associated with the shallow intra-bandgap defect states arising from the presence of oxygen vacancies [25], we thus determined the onsets of the O K-edge EELS spectra using the signal intensity at the first inflection point in the O K-edge EELS spectrum of the reference sample (Fig. 4b). This substantially ensures the onset of the NW O K-edge EELS spectrum represents the intrinsic CBM of the α-Fe_2O_3 NW.

Peaks A1 and A2 in the O K-edge EELS spectra are known as pre-peaks and are respectively related to the t_{2g} and e_g bands of α-Fe_2O_3 [26]. Horizontally aligning the onsets of the O K-edge EELS spectra (Fig. 4c), we observed that the NW spectrum revealed a ~0.05-eV relative right shift at peak A1 and a ~0.1-eV relative left shift at peak A2. Because the $(FeO_6)^{9-}$ octahedral units in α-Fe_2O_3 are actually trigonally distorted from octahedral symmetry, in a crystal-field-based scenario, the t_{2g} band is further split into two sub-bands designated as a_{1g} and $e_g(\pi)$. The electronic orbitals of the a_{1g} sub-band lie parallel to the c-axis of α-Fe_2O_3, while the orbitals of the $e_g(\pi)$ sub-band perpendicular to it [27,28]. This fact makes the position of peak A1 to be associated with the sample orientation (for normal STEM-EELS, where the collection semi-angle is significantly larger than the O K-edge characteristic angle, the overall electron momentum transfer is predominantly along directions perpendicular to the incident electron beam). According to our EELS experiment condition, the c-axis momentum transfer for the incident electrons takes a smaller signal contribution weight in the NW O K-edge EELS spectrum than in the O K-edge EELS spectrum of the reference sample. Therefore, it is possible that peak A1 in the NW O K-edge EELS spectrum is centered closer to the position corresponding to the $e_g(\pi)$ sub-band and so slightly further from the onset. Because the trigonal distortion of the $(FeO_6)^{9-}$ octahedral units does not cause a

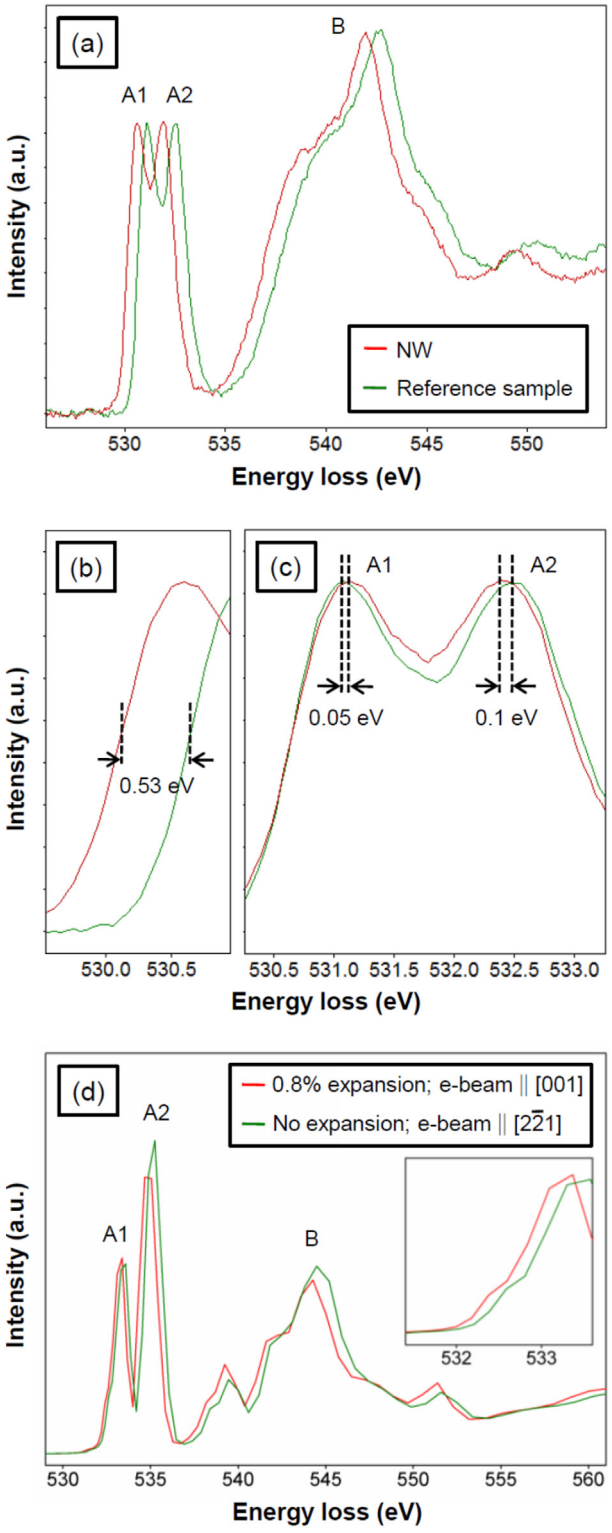

Fig. 4. (a) O K-edge EELS spectra of an as-synthesized α-Fe_2O_3 NW with (001) basal faces and a stoichiometric α-Fe_2O_3 reference sample. (b) Signal threshold regions in the spectra in (a). The dashed lines mark the determined onset positions. (c) Pre-peak regions in the spectra in (a); the NW spectrum has been shifted horizontally from its original position to compensate for the difference in the onset energy. (d) Simulated O K-edge EELS spectra of α-Fe_2O_3 with and without 0.8% lattice expansion. The inset shows the enlarged image of the spectrum onset regions in the simulated spectra.

substantial split of the e_g band [29], the position of peak A2 is independent of the sample orientation. Hence, the observed relative shift at peak A2 indicates the difference in energy between the e_g band and the CBM for the α-Fe_2O_3 NW is smaller than that for pristine α-Fe_2O_3. Since, for the energy band structure of α-Fe_2O_3, the CBM is equivalent to the bottom edge of the t_{2g} band, this finding indicates that the α-Fe_2O_3 NW exhibits a diminished octahedral ligand field splitting. Essentially, this can be attributed to reduced Fe 3d-O 2p orbital hybridization [26] and so means the average Fe—O interatomic distance in the α-Fe_2O_3 NW is larger [30].

According to the real-space multiple-scattering theory, forming the main peak (i.e., peak B in Fig. 4a) in an O K-edge core-excitation spectrum of α-Fe_2O_3 is a result of scattering resonances each govern by the first oxygen shell around an excited oxygen anion [31]. If the spectrum onset is defined as the energy level of zero kinetic energy for the ejected core electrons, the difference in energy between the main peak and the spectrum onset should retain the relation in Eq. (1) when the α-Fe_2O_3 lattice is slightly distorted [31].

$$\Delta E \times R^2 = \text{constant} \quad (1)$$

where ΔE is the energy difference, and R represents the average radius of the first oxygen shell. The values of ΔE in the O K-edge EELS spectra of the NW and reference sample were measured to be 11.8 and 12.0 eV, respectively. This means that the average O—O interatomic distance in the α-Fe_2O_3 NW is 0.8% longer than in pristine α-Fe_2O_3. Because the lattice framework of α-Fe_2O_3 is comprised of oxygen anions, this further suggests the lattice of the α-Fe_2O_3 NW is expanded relative to that of pristine α-Fe_2O_3. Another indication of the presence of lattice expansion in the α-Fe_2O_3 NW is the energy shift between the O K-edge EELS spectrum onsets (measured to be 0.53 eV). Since the ionicity of α-Fe_2O_3 is high [32], the energy of the O 1s core electrons in α-Fe_2O_3 should be sensitive to variations in the average Fe—O interatomic distance [33]. More specifically, it is believed an expansion in the α-Fe_2O_3 lattice parameters, which corresponds to an increase in the average Fe—O interatomic distance in α-Fe_2O_3, will cause a greater increase in the O 1s electron energy and a smaller decrease in the CBM energy, thereby leading to a downshift in the O K-edge onset. To verify this, we have simulated the O K-edge EELS spectra of α-Fe_2O_3 with and without 0.8% lattice expansion (see supplementary information for the detail). The simulation results in Fig. 4d clearly indicate that lattice expansion results in a downfield shift in the O K-edge onset of α-Fe_2O_3. Note that the onset shift in the simulated spectra (~0.15 eV) is smaller than in the experimental spectra. A possible reason accounting for this is that only uniform lattice expansion was considered in simulating the O K-edge EELS spectrum of lattice-expanded α-Fe_2O_3.

Through an EELS-based stoichiometric comparison between an as-synthesized α-Fe_2O_3 NW with (001) basal faces and the reference sample (Fig. S7), we verified the synthesized α-Fe_2O_3 NWs with (001) basal faces were oxygen-deficient. However, since the difference in specimen thickness might introduce uncertainty into the stoichiometric comparison, examining whether a chemical shift [34] is present at the Fe $L_{2,3}$-edge core excitation of the α-Fe_2O_3 NWs helps reconfirm the oxygen deficiency in them, for which monochromated dual-EELS is an effective practical approach. The Fe $L_{2,3}$-edge EELS spectra of an as-synthesized α-Fe_2O_3 NW with (001) basal faces and the reference sample are shown in Fig. 5a. The two spectra have been normalized to the maximum of the first L_3-edge peak, and their onsets were determined with the same procedure used to determine the onsets of the O K-edge EELS spectra. It was found that the onset of the Fe $L_{2,3}$-edge EELS spectrum of the NW is ~0.15 eV lower than that of the reference sample (Fig. 5b). Because the comparison benchmark was the spectrum onset, the near-edge fine structure variation associated with the lattice distortion and sample orientation difference was not a crucial factor affecting our edge shift determination. Therefore, the measured energy shift should be substantially attributed to a combination of the energy variations of the Fe $2p_{3/2}$ core electrons and the CBM (for α-Fe_2O_3, the Fe $L_{2,3}$-edge onset is also linked with the CBM). In light of the high ionicity of α-Fe_2O_3, just like the aforesaid O K-edge situation, the energy of the Fe

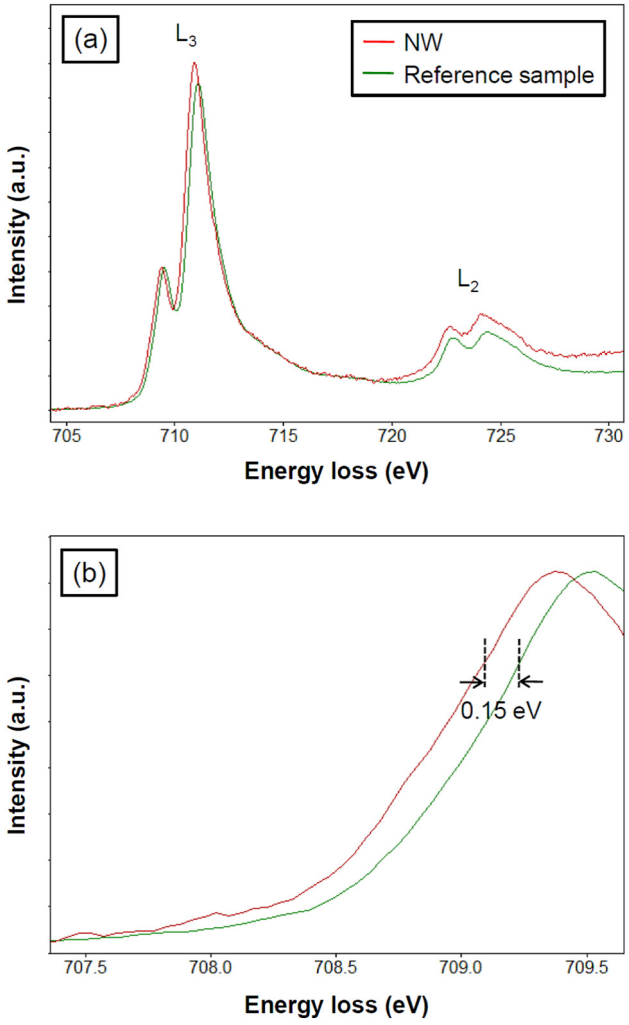

Fig. 5. (a) Fe $L_{2,3}$-edge EELS spectra of an as-synthesized α-Fe_2O_3 NW with (001) basal faces and the reference sample. (b) Signal threshold regions in the spectra in (a). The dashed lines mark the onset positions.

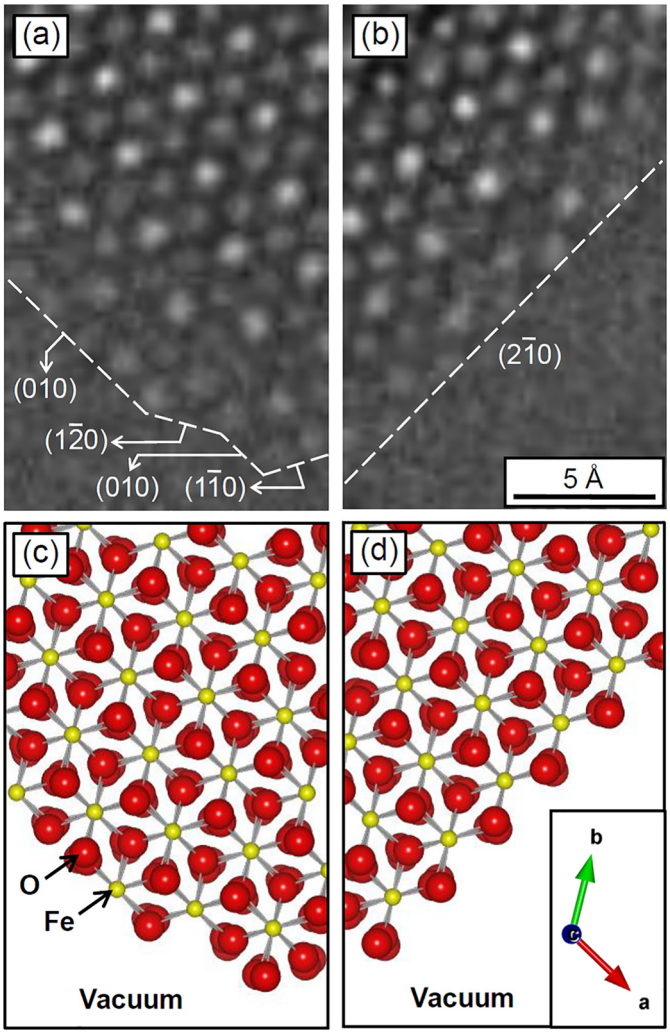

Fig. 6. Enlarged images of the areas within the red dashed box (a) and the red dotted box (b) in Fig. 3a. (c) and (d) Structural models respectively correspond to (a) and (b).

$2p_{3/2}$ core electrons is more sensitive to lattice expansion than the CBM energy does. This implies the tensile strain in the α-Fe_2O_3 NW will cause its Fe $L_{2,3}$-edge onset higher in energy than that of pristine α-Fe_2O_3. Therefore, ruling out the strain-related factor, we believe the energy shift between the Fe $L_{2,3}$-edge EELS spectrum onsets is essentially a chemical shift which indicates the iron cations in the α-Fe_2O_3 NW are reduced.

In the present study, we adopted an atmospheric thermal oxidation process to synthesize α-Fe_2O_3 NWs. Hence, oxygen deficiency in the studied α-Fe_2O_3 NWs is not likely caused by an insufficient oxygen supply during the NW growth. Further evidence of this was obtained by inspecting the edge surface termination of the α-Fe_2O_3 NWs. As representative examples, the enlarged images and corresponding structural models of the areas within the red dashed and red dotted boxes in Fig. 3a are shown in Fig. 6. It can be observed that the NW edge terminates with either the (110)-type or (100)-type facets. More importantly, the surface atom configurations at the NW edge are consistent with the stoichiometric predictions [35], meaning the α-Fe_2O_3 NWs indeed grew with a sufficient oxygen supply. This fact strongly indicates that the emergence of oxygen vacancies in α-Fe_2O_3 NWs with (001) basal faces synthesized via thermal oxidation of iron-based substrates is a consequence of tensile strain.

For the sequential oxide formation in synthesizing α-Fe_2O_3 NWs via the thermal oxidation route [5], the topoaxial relation between the α-Fe_2O_3 scale layer and the Fe_3O_4 scale layer has been verified to be α-Fe_2O_3 [001]∥Fe_3O_4 [111] [36]. That is to say, the two phases joint on the basis of either superposing or coupling of the close-packed oxygen planes. The average interatomic distance between adjacent oxygen anions in a close-packed oxygen plane of Fe_3O_4 is approximately 2% larger than that of α-Fe_2O_3. This means the underlying Fe_3O_4 scale layer generates tensile stress in the α-Fe_2O_3 scale layer. Because the tensile stress within the thin dense α-Fe_2O_3 scale layer is not effectively relaxed, it then causes tensile strain in the α-Fe_2O_3 NWs forming above the α-Fe_2O_3 scale layer. It is now known that, of the growing α-Fe_2O_3 NWs, those with (001) basal faces exhibit a strain accommodation pattern composed of lattice distortion and periodic (3$\bar{3}$0) gap expansions induced by oxygen vacancy accumulations (Fig. 7). The emergence of the induced (3$\bar{3}$0) gap expansions is reasonable from a thermodynamic perspective, because forming oxygen vacancies offers an effective route to reduce the strain energy; also, the interaction energy of oxygen vacancies is reduced through aggregation, which has been pointed out by Ong et al. in a study of $SrCrO_{3-\delta}$ [37]. Owing to the effects of strain field and charge repulsion, the induced (3$\bar{3}$0) gap expansions repel one another. Their distribution period within a local range is expected to be governed by the repulsive forces between them. A similar phenomenon is seen in $SrCrO_{3-\delta}$, in which repulsion between the oxygen-deficient planes results in an ordering arrangement [37]. Since the degree of local strain in the α-Fe_2O_3 NWs with (001) basal faces is thickness-dependent, the strain/electrical fields of the induced (3$\bar{3}$0) gap expansions are related to the local NW thickness. This means that

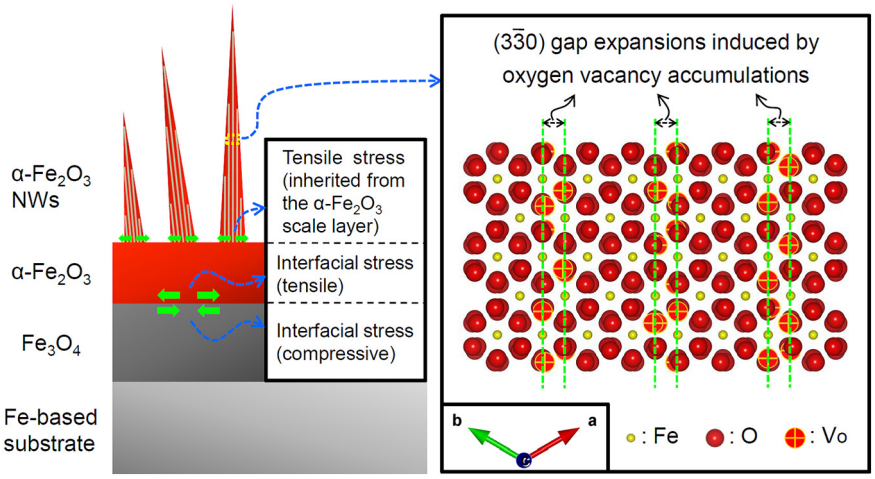

Fig. 7. Formation mechanism of the periodic (3$\bar{3}$0) gap expansions induced by oxygen vacancy accumulations. Vo stands for oxygen vacancy.

different defect periodicities can exist within a single α-Fe_2O_3 NW provided that the thickness of the NW edge and the NW bulk are sufficiently different.

As a technical advance in HR-TEM imaging, NCSI is an efficient and spatially precise technique [23] for investigating oxygen column displacements in strained metal oxides. Remedying the limitations of HR-TEM/STEM imaging, core-loss EELS is capable of analyzing the strain-induced microchemical variations in strained metal oxides. However, when the strain is minimal, feature changes in the EELS spectra are usually too subtle for typical EELS with a ~1 eV FWHM energy resolution [38]. This limitation underscores the need to reduce the energy spread of the electron beam to the sub-eV level. Via this study, we have demonstrated the applicability of integrating NCSI and monochromated EELS for the analysis of strain-induced microstructural and microchemical variations in lightly strained metal oxides. It is believed this advanced technical integration can be an effective material characterization strategy for strain-based oxygen vacancy engineering [39,40].

4. Conclusions

α-Fe_2O_3 NWs with (001) basal faces were synthesized using an atmospheric thermal oxidation process. With NCSI and atomic-column position analysis, we observed thickness-dependent tensile strain in the α-Fe_2O_3 NWs and revealed that the ordered structure within the NWs was periodic (3$\bar{3}$0) gap expansions induced by oxygen vacancy accumulations. The HR-TEM investigation findings were further confirmed in the monochromated O K-edge and Fe $L_{2,3}$-edge EELS analysis. The O K-edge EELS result shows that the average Fe—O and O—O interatomic distances in the α-Fe_2O_3 NWs are larger than they are in pristine α-Fe_2O_3. The Fe $L_{2,3}$-edge EELS result provides evidence of oxygen deficiency in the α-Fe_2O_3 NWs. The α-Fe_2O_3 NWs possess a stoichiometric surface termination, which indicates that the oxygen deficiency is not caused by an insufficient oxygen supply during the NW growth. Therefore, forming the ordered structure in the α-Fe_2O_3 NWs is a result of to create a thermodynamically preferred route for accommodating the tensile strain. With this work, we demonstrate the applicability of integrating NCSI and monochromated EELS for characterizing lightly strained metal oxides.

CRediT authorship contribution statement

Ming-Wei Lai: Conceptualization, Methodology, Investigation, Writing - original draft, Writing - review & editing. **Hiroki Kurata:** Conceptualization, Writing - original draft, Writing - review & editing, Supervision.

Declaration of competing interest

The authors declare that they have no known competing financial interests or personal relationships that could have appeared to influence the work reported in this paper.

Acknowledgment

This work was supported by a Grant-in-Aid for Scientific Research (Grant Number: 17H02739) from the Ministry of Education, Culture, Sports, Science and Technology (MEXT) of Japan, the Core-to-Core Program (A. Advanced Research Networks) of the Japan Society for the Promotion of Science (JSPS).

Data availability statement

The data that support the findings of the present study are included within the article and its supplementary information. Other related data are available from the corresponding author upon request.

Appendix A. Supplementary information

Supplementary information to this article can be found online at https://doi.org/10.1016/j.matdes.2020.108596.

References

[1] K. Sivula, F. Le Formal, M. Grätzel, Solar water splitting: progress using hematite (α-Fe_2O_3) photoelectrodes, ChemSusChem 4 (2011) 432–449.
[2] X. Wen, S. Wang, Y. Ding, Z.L. Wang, S. Yang, Controlled growth of large-area, uniform, vertically aligned arrays of α-Fe_2O_3 nanobelts and nanowires, J. Phys. Chem. B 109 (2005) 215–220.
[3] Y.-L. Chueh, M.-W. Lai, J.-Q. Liang, L.-J. Chou, Z.L. Wang, Systematic study of the growth of aligned arrays of α-Fe_2O_3 and Fe_3O_4 nanowires by a vapor-solid process, Adv. Funct. Mater. 16 (2006) 2243–2251.
[4] Y. Xie, Y. Ju, Y. Toku, Y. Morita, Fabrication of Fe_2O_3 nanowire arrays based on oxidation-assisted stress-induced atomic-diffusion and their photovoltaic properties for solar water splitting, RSC Adv. 7 (2017) 30548–30553.
[5] L. Yuan, Y. Wang, R. Cai, Q. Jiang, J. Wang, B. Li, A. Sharma, G. Zhou, The origin of hematite nanowire growth during the thermal oxidation of iron, Mater. Sci. Eng. B 177 (2012) 327–336.
[6] Y.-C. Lee, Y.-L. Chueh, C.-H. Hsieh, M.-T. Chang, L.-J. Chou, Z.L. Wang, Y.-W. Lan, C.-D. Chen, H. Kurata, S. Isoda, p-Type α-Fe_2O_3 nanowires and their n-type transition in a reductive ambient, Small 3 (2007) 1356–1361.
[7] T. Li, H. Feng, Y. Wang, C. Wang, W. Zhu, L. Yuan, G. Zhou, Formation of modulated structures induced by oxygen vacancies in α-Fe_2O_3, J. Cryst. Growth 498 (2018) 10–16.
[8] J. Mock, B. Klingebiel, F. Köhler, M. Nuys, J. Flohre, S. Muthmann, T. Kirchartz, R. Carius, Oxygen vacancy doping of hematite analyzed by electrical conductivity and thermoelectric power measurements, Phys. Rev. Mater. 1 (2017) 065407.

[9] J. Hu, X. Zhao, W. Chen, Z. Chen, Enhanced charge transport and increased active sites on α-Fe_2O_3 (110) nanorod surface containing oxygen vacancies for improved solar water oxidation performance, ACS Omega 3 (2018) 14973–14980.
[10] M. Forster, R.J. Potter, Y. Ling, Y. Yang, D.R. Klug, Y. Li, A.J. Cowan, Oxygen deficient α-Fe_2O_3 photoelectrodes: a balance between enhanced electrical properties and trap-mediated losses, Chem. Sci. 6 (2015) 4009–4016.
[11] Z. Chen, U. Cvelbar, M. Mozetič, J. He, M.K. Sunkara, Long-range ordering of oxygen-vacancy planes in α-Fe_2O_3 nanowires and nanobelts, Chem. Mater. 20 (2008) 3224–3228.
[12] U. Aschauer, R. Pfenninger, S.M. Selbach, T. Grande, N.A. Spaldin, Strain-controlled oxygen vacancy formation and ordering in $CaMnO_3$, Phys. Rev. B 88 (2013) 54111.
[13] C.-L. Jia, M. Lentzen, K. Urban, High-resolution transmission electron microscopy using negative spherical aberration, Microsc. Microanal. 10 (2004) 174–184.
[14] K.W. Urban, C.-L. Jia, L. Houben, M. Lentzen, S.-B. Mi, K. Tillmann, Negative spherical aberration ultrahigh-resolution imaging in corrected transmission electron microscopy, Phil. Trans. R. Soc. A 367 (2009) 3735–3753.
[15] C.-L. Jia, S.-B. Mi, L. Jin, Quantitative HRTEM and its application in the study of oxide materials, Chin. Phys. B 27 (2018) 056803.
[16] P. Rajak, M. Islam, J.J. Jiménez, J.M. Mánuel, P. Aseev, Ž. Gačević, E. Calleja, R. García, F.M. Morales, S. Bhattacharyya, Unravelling the polarity of InN quantum dots using a modified approach of negative-spherical-aberration imaging, Nanoscale 11 (2019) 13632–13638.
[17] J. Scott, P.J. Thomas, M. MacKenzie, S. McFadzean, J. Wilbrink, A.J. Craven, W.A.P. Nicholson, Near-simultaneous dual energy range EELS spectrum imaging, Ultramicroscopy 108 (2008) 1586–1594.
[18] P. Galindo, J. Pizarro, S. Molina, K. Ishizuka, High resolution peak measurement and strain mapping using peak pairs analysis, Microsc. Anal. 23 (2009) 23–25.
[19] W.S. Choi, J.-H. Kwon, H. Jeen, J.E. Hamann-Borrero, A. Radi, S. Macke, R. Sutarto, F. He, G.A. Sawatzky, V. Hinkov, M. Kim, H.N. Lee, Strain-induced spin states in atomically ordered cobaltites, Nano Lett. 12 (2012) 4966–4970.
[20] S.V. Kalinin, N.A. Spaldin, Functional ion defects in transition metal oxides, Science 341 (2013) 858–859.
[21] Y.-M. Kim, J. He, M.D. Biegalski, H. Ambaye, V. Lauter, H.M. Christen, S.T. Pantelides, S.J. Pennycook, S.V. Kalinin, A.Y. Borisevich, Probing oxygen vacancy concentration and homogeneity in solid-oxide fuel-cell cathode materials on the subunit-cell level, Nat. Mater. 11 (2012) 888–894.
[22] J. Gazquez, S. Bose, M. Sharma, M.A. Torija, S.J. Pennycook, C. Leighton, M. Varela, Lattice mismatch accommodation via oxygen vacancy ordering in epitaxial $La_{0.5}Sr_{0.5}CoO_{3-\delta}$ thin films, APL Mater. 1 (2013), 012105.
[23] N. Gauquelin, K.H.W. van den Bos, A. Béché, F.F. Krause, I. Lobato, S. Lazar, A. Rosenauer, S. Van Aert, J. Verbeeck, Determining oxygen relaxations at an interface: a comparative study between transmission electron microscopy techniques, Ultramicroscopy 181 (2017) 178–190.
[24] B. Gilbert, C. Frandsen, E.R. Maxey, D.M. Sherman, Band-gap measurements of bulk and nanoscale hematite by soft x-ray spectroscopy, Phys. Rev. B 79 (2009), 035108.
[25] Z. Zhou, J. Liu, R. Long, L. Li, L. Guo, O.V. Prezhdo, Control of charge carriers trapping and relaxation in hematite by oxygen vacancy charge: *ab initio* non-adiabatic molecular dynamics, J. Am. Chem. Soc. 139 (2017) 6707–6717.
[26] F.M.F. de Groot, M. Grioni, J.C. Fuggle, J. Ghijsen, G.A. Sawatzky, H. Petersen, Oxygen 1s x-ray-absorption edges of transition-metal oxides, Phys. Rev. B 40 (1989) 5715–5723.
[27] C.X. Kronawitter, I. Zegkinoglou, S. Shen, J. Guo, F.J. Himpsel, S.S. Mao, L. Vayssieres, On the orbital anisotropy in hematite nanorod-based photoanodes, Phys. Chem. Chem. Phys. 15 (2013) 13483–13488.
[28] J.B. Goodenough, Metallic oxides, Prog. Solid State Chem. 5 (1971) 145–399.
[29] A. Bandyopadhyay, J. Velev, W.H. Butler, S.K. Sarker, O. Bengone, Effect of electron correlations on the electronic and magnetic structure of Ti-doped α-hematite, Phys. Rev. B 69 (2004) 174429.
[30] W.A. Harrison, Electronic Structure and the Properties of Solids, Dover, New York, 1989.
[31] Z.Y. Wu, S. Gota, F. Jollet, M. Pollak, M. Gautier-Soyer, C.R. Natoli, Characterization of iron oxides by x-ray absorption at the oxygen K edge using a full multiple-scattering approach, Phys. Rev. B 55 (1997) 2570–2577.
[32] M. Lenglet, Iono-covalent character of the metal-oxygen bonds in oxides: a comparison of experimental and theoretical data, Act. Passive Electron. Compon. 27 (2004) 1–60.
[33] P.S. Bagus, F. Illas, G. Pacchioni, F. Parmigiani, Mechanisms responsible for chemical shifts of core-level binding energies and their relationship to chemical bonding, J. Electron Spectrosc. Relat. Phenom. 100 (1999) 215–236.
[34] H. Tan, J. Verbeeck, A. Abakumov, G. Van Tendeloo, Oxidation state and chemical shift investigation in transition metal oxides by EELS, Ultramicroscopy 116 (2012) 24–33.
[35] H. Guo, A.S. Barnard, Thermodynamic modelling of nanomorphologies of hematite and goethite, J. Mater. Chem. 21 (2011) 11566–11577.
[36] H. Srivastava, A.K. Srivastava, M. Babu, S. Rai, T. Ganguli, Topotaxial growth of α-Fe_2O_3 nanowires on iron substrate in thermal annealing method, J. Appl. Phys. 119 (2016), 244311.
[37] P.-V. Ong, Y. Du, P.V. Sushko, Low-dimensional oxygen vacancy ordering and diffusion in $SrCrO_{3-\delta}$, J. Phys. Chem. Lett. 8 (2017) 1757–1763.
[38] R.F. Egerton, Electron energy-loss spectroscopy in the TEM, Rep. Prog. Phys. 72 (2009), 016502.
[39] A. Herklotz, D. Lee, E.-J. Guo, T.L. Meyer, J.R. Petrie, H.N. Lee, Strain coupling of oxygen non-stoichiometry in perovskite thin films, J. Phys. Condens. Matter 29 (2017), 493001.
[40] R.U. Chandrasena, W. Yang, Q. Lei, M.U. Delgado-Jaime, K.D. Wijesekara, M. Golalikhani, B.A. Davidson, E. Arenholz, K. Kobayashi, M. Kobata, F.M.F. de Groot, U. Aschauer, N.A. Spaldin, X. Xi, A.X. Gray, Strain-engineered oxygen vacancies in $CaMnO_3$ thin films, Nano Lett. 17 (2017) 794–799.